

Application of Spectral Polarimetry to a Hailstorm at Low Elevation Angle

YADONG WANG

Department of Electrical and Computer Engineering, Southern Illinois University at Edwardsville, Edwardsville, Illinois

TIAN-YOU YU

School of Electrical and Computer Engineering, and Advanced Radar Research Center, and School of Meteorology, University of Oklahoma, Norman, Oklahoma

ALEXANDER V. RYZHKOV

Advanced Radar Research Center, and School of Meteorology, and Cooperative Institute for Mesoscale Meteorological Studies, University of Oklahoma, Norman, Oklahoma

MATTHEW R. KUMJIAN

Department of Meteorology and Atmospheric Science, The Pennsylvania State University, University Park, Pennsylvania

(Manuscript received 9 July 2018, in final form 2 January 2019)

ABSTRACT

Spectral polarimetry has the potential to be used to study microphysical properties in relation to the dynamics within a radar resolution volume by combining Doppler and polarimetric measurements. The past studies of spectral polarimetry have focused on using radar measurements from higher elevation angles, where both the size sorting from the hydrometeors' terminal velocities and polarimetric characteristics are maintained. In this work, spectral polarimetry is applied to data from the 0° elevation angle, where polarimetric properties are maximized. Radar data collected by the C-band University of Oklahoma Polarimetric Radar for Innovations in Meteorology and Engineering (OU-PRIME) during a hailstorm event on 24 April 2011 are used in the analysis. The slope of the spectral differential reflectivity exhibits interesting variations across the hail core, which suggests the presence of size sorting of hydrometeors caused by vertical shear in a turbulent environment. A nearby S-band polarimetric Weather Surveillance Radar-1988 Doppler (KOUN) is also used to provide insights into this hailstorm. Moreover, a flexible numerical simulation is developed for this study, in which different types of hydrometeors such as rain and melting hail can be considered individually or as a combination under different sheared and turbulent conditions. The impacts of particle size distribution, shear, turbulence, attenuation, and mixture of rain and melting hail on polarimetric spectral signatures are investigated with the simulated Doppler spectra and spectral differential reflectivity.

1. Introduction

Polarimetric weather radar has shown its capabilities in improving quantitative precipitation estimation, hydrometeor classification, data quality control, and severe weather detection and forecasting (e.g., Meischner 2003; Ryzhkov et al. 2005; Park et al. 2009; Scharfenberg et al. 2005; Kumjian 2013a,b; Chandrasekar et al. 2013; Wang and Yu 2015; Hwang et al. 2017). Polarimetric variables such as differential reflectivity Z_{DR} , correlation coefficient ρ_{HV} , and differential phase ϕ_{DP} can provide information

about hydrometeor's size, shape, concentration, orientation, and type. Kinematic features such as convective storm updrafts, vertical wind shear, and storm-relative helicity can be inferred from prominent polarimetric signatures such as the Z_{DR} column and the Z_{DR} arc (e.g., Kumjian and Ryzhkov 2008, 2009, 2012). In addition, the kinematic information such as storm intensity, motion, and turbulence can also be derived from Doppler measurements of mean radial velocity and spectrum width. These polarimetric and Doppler variables contain either the dynamical or the microphysical properties that are integrated over the radar resolution volume. Spectral polarimetry, on the other hand, can unveil the polarimetric

Corresponding author: Yadong Wang, yadwang@siue.edu

DOI: 10.1175/JTECH-D-18-0115.1

© 2019 American Meteorological Society. For information regarding reuse of this content and general copyright information, consult the [AMS Copyright Policy](http://www.ametsoc.org/PUBSReuseLicenses) (www.ametsoc.org/PUBSReuseLicenses).

variables directly as a function of radial velocities within one resolution volume (e.g., Unal et al. 2001; Russchenberg et al. 2008; Yu et al. 2012), and this provides a unique opportunity to relate storm microphysical properties to kinematics. As shown in Doviak and Zrnić (1993), the Doppler spectrum describes the returned power as a function of radial velocities, and the power at each velocity bin is contributed by all scatterers with the same radial velocity within the radar resolution volume. Similarly, spectral differential reflectivity represents a spectrum of differential reflectivity, and the value at each bin is determined by the ratio of returned power between horizontal (H) and vertical (V) polarizations from all the scatterers with the same radial velocity. Additionally, spectral correlation coefficient and spectral differential phase can be understood in the same manner. Therefore, if the relation between hydrometeor sizes and radial velocities can be established (i.e., size sorting is present), spectral polarimetry can reveal the polarimetric properties as a function of hydrometeor sizes. Note that polarimetric variables can still be obtained from these polarimetric spectra through integrating the whole resolution volume (Yu et al. 2012).

Since hydrometeors from different species and sizes possess different terminal velocities (Atlas et al. 1973), past studies using spectral polarimetry mainly relied on size sorting originating from hydrometeors' different terminal velocities. For vertically pointing radar observations, this size sorting is maximized; however, hydrometeors (such as raindrops) viewed from below produce 0 dB Z_{DR} . Another extreme case is for 0° elevation angle, where Z_{DR} magnitudes are maximized but size sorting is totally diminished because of the same radial velocity (background wind) from all sizes of hydrometeors. Thus, spectral polarimetry typically has focused on using measurements from higher elevation angles where both the size sorting from the hydrometeors' terminal velocities and the polarimetric characteristics are maintained. For example, Spek et al. (2008) retrieved the particle size distributions of two mixed ice particles, background wind, and turbulence by applying spectral polarimetry to S-band data collected at 45° elevation angle. Moisseev et al. (2006) applied spectral polarimetry to estimate the shape parameter of raindrops using data from the S-band CSU-CHILL at elevation of 30° and the S-band Transportable Atmospheric Radar (TARA) at 45°.

In addition to different terminal velocities, hydrometeor size sorting can be maintained by different mechanisms, including convective updrafts and nonzero storm-relative flow associated with vertical wind shear (e.g., Kumjian and Ryzhkov 2012; Dawson et al. 2014, 2015). In this work, spectral polarimetry was applied to a hailstorm

observed by one C-band polarimetric radar at 0° elevation angle, where no size sorting should be expected if only the terminal speed of hydrometeors and the uniform background wind are considered. However, it was observed that spectral differential reflectivity exhibits different patterns in different regions of the storm, which suggests the presence of a different ongoing size sorting mechanisms. It is hypothesized that the variation of the observed spectral differential reflectivity is a result of shear-induced size sorting from raindrops and melting hailstones in a turbulent environment. The idea of a hydrometeor's trajectory in a sheared environment was first proposed by Marshall (1953), and its velocity is derived to be a function of its terminal velocity and environmental vertical shear (e.g., Brussaard 1974). Therefore, we hypothesize that when the vertical shear is present, the size-dependent velocity of hydrometeors can be revealed in polarimetric spectra even at 0° elevation angle. This work therefore focuses on the interplay of microphysics and kinematics within the resolution volume. The hypothesis will be qualitatively supported from the analysis of radar observations, mesonet data, and storm reports. The impact of shear, turbulence, particle size distributions of rain and melting hail, and attenuation on the slope of spectral differential reflectivity will be investigated using simulations.

In this paper, observations of a hailstorm from nearby S-band and C-band polarimetric radars are first presented in section 2. In addition, the variation of spectral differential reflectivity revealed from the application of spectral polarimetry to C-band data at 0° elevation angle is shown. In section 3, a brief overview of size sorting in a sheared environment is provided. To further investigate the cause of these variations of spectral differential reflectivity, a simulation is developed in section 4, where two cases of rain and a mixture of rain and melting hail are examined. A summary and conclusions are provided in section 5.

2. Observations of a hailstorm on 24 April 2011

A total of 40 hailstorms were reported in Oklahoma on 24 April 2011, which cost approximately \$65,000 (U.S. dollars) in property damage over 19 affected counties (<http://www.ncdc.noaa.gov/stormevents>). One of the hailstorms is of special interest, because it was observed simultaneously by two nearby polarimetric radars, the C-band University of Oklahoma Polarimetric Radar for Innovations in Meteorology and Engineering (OU-PRIME) (Palmer et al. 2011) and an S-band polarimetric Weather Surveillance Radar-1988 Doppler (WSR-88D) in Norman, Oklahoma (KOUN). The storm was located within 60-km range from both radars during

the time of interest. The level I in-phase and quadrature-phase (I and Q) signals from the OU-PRIME were collected, which allows the implementation of spectral polarimetry. A more detailed description of the observations is presented in the following subsection.

a. Dual-wavelength observations

The C-band OU-PRIME is located approximately 6.78 km southeast of the S-band KOUN, and both of them are dual-polarization radars operating in simultaneous transmission and reception mode. A detailed comparison of the specifications between OU-PRIME and KOUN is provided in Picca and Ryzhkov (2012). Even though the scanning strategy and resolution are not the same for these two radars, valuable information can be obtained by the simultaneous observations from the two different wavelengths. For example, Borowska et al. (2011) studied the attenuation and differential attenuation from melting hail using these two different wavelengths radars. Picca and Ryzhkov (2012) used simultaneous OU-PRIME and KOUN data to study the hail size estimation and hail signatures near surface and aloft. In addition, Bodine et al. (2014) used these two radars to investigate tornado debris signatures from an EF4 (on the enhanced Fujita scale) tornado.

Between 1700:13 and 1959:49 UTC, the OU-PRIME was operated with alternating plan position indicator (PPI) and range–height indicator (RHI) scans. In the PPI mode, a total of eight elevations were completed in approximately 2 min with a pulse repetition time (PRT) of 0.8475 ms. In the RHI mode, OU-PRIME scanned from 0° to 20° in elevation at the azimuth angle of 233.3° in approximately 52 s using the same PRT. The KOUN radar was operated with volume coverage pattern (VCP) 12 (4.5-min update time) during that period. Comparisons of PPI scans from OU-PRIME at 0° elevation angle (left panels) and KOUN at 0.5° elevation angle (right panels) both at 1856:07 UTC are shown in Fig. 1. The top (Figs. 1a,b) and middle rows (Figs. 1c,d) are the fields of reflectivity Z and Z_{DR} , and the field of ρ_{HV} from OU-PRIME is shown in Fig. 1e. The result of hydrometeor classification algorithm (HCA) (Park et al. 2009) from KOUN is shown in Fig. 1f, where ground clutter (GC), biological scatterers (BI), dry snow (DS), wet snow (WS), crystals (CR), graupel (GR), big drops (BD), light/moderate rain (RA), heavy rain (HR), mixture of rain and hail (HA), and unknown (UK) are shown (Park et al. 2009). The locations of both radars are denoted by white asterisks. The azimuthal direction of OU-PRIME's RHI scan is also included and denoted by a solid black line. Note that all the KOUN data have been transformed into the same coordinates as OU-PRIME

data; therefore, they have the same origin to facilitate the comparison.

Despite the generally similar Z and Z_{DR} contours from these two radars, enhanced reflectivity (>60 dBZ) and differential reflectivity (>4 dB) can be observed from OU-PRIME such as at approximately $(-40, -32)$, $(-40, 0)$, and $(-20, 5)$ km (Figs. 1a,c). The ρ_{HV} values at these regions (Fig. 1d) are as low as 0.8 from the C-band OU-PRIME, whereas relatively high values from the S-band KOUN are still maintained (not shown). These comparisons suggest the presence of resonance scattering effects caused by large drops and small melting hail at C band (Picca and Ryzhkov 2012). According to a storm report from the National Oceanic and Atmospheric Administration (<http://www.ncdc.noaa.gov/stormevents>), hailstones of 1.9-cm size were observed at 1850 UTC in Rush Spring (about 50 km southwest from OU-PRIME; annotated in Fig. 1), which can further support the fact of hail.

At 1858:21 UTC, OU-PRIME switched to RHI scan at azimuth angle of 233.3°, and the fields from Z , Z_{DR} , and ρ_{HV} are presented in Figs. 2a, 2c, and 2e. For comparison purposes, data from the KOUN volume scan at 1856:07 UTC were interpolated to the same locations as in the OU-PRIME's RHI scan using a nearest neighborhood method; the interpolated Z and Z_{DR} are shown on the right top two panels of Figs. 2b and 2d. Additionally, the HCA results obtained using those interpolated data are shown in Fig. 2f. The resonance effects at C band are still evident in the region at ranges between 48 and 52 km and altitude below 1.5 km, which is manifested by enhanced Z (>55 dBZ) and Z_{DR} (>4 dB), and reduced ρ_{HV} (<0.89) when compared to S-band data (Borowska et al. 2011; Picca and Ryzhkov 2012).

Differential attenuation at C band is evident after 52 km, where OU-PRIME Z_{DR} falls below -3.5 dB at ranges of approximately 54 to 57 km. The Z_{DR} from S-band KOUN is approximately 2–3 dB at similar ranges. Such anomalous attenuation at the C band is likely a result of large raindrops and melting hail (Meischner et al. 1991; Ryzhkov et al. 2007; Anderson et al. 2011; Ryzhkov et al. 2013). Moreover, HA was identified by KOUN at ranges around 50 to 55 km and at altitudes between 1 and 4 km. Note that the mixture of hail and rain was not directly identified at lower elevations, which may be a result of the time difference between these two observations or errors in the hydrometeor classification algorithm. It is speculated that the synthesized KOUN radial at 1856:07 UTC only samples the edge of the storm core, as suggested by the HCA results in Fig. 1. In summary, the analysis of the observations from the two wavelengths strongly suggests the presence of a mixture of hail and rain and large drops in the lowest elevation

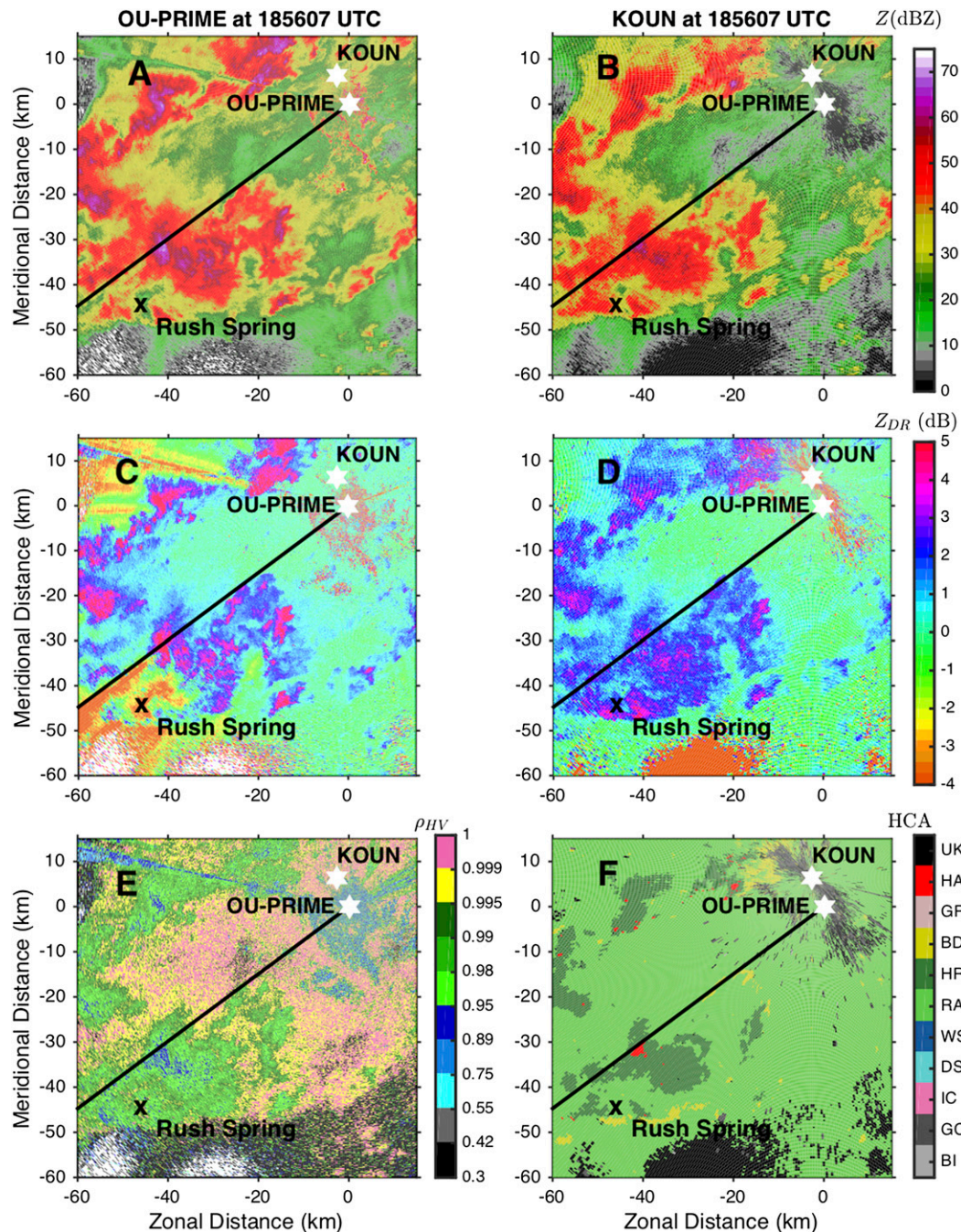


FIG. 1. The hailstorm observed by the PPI scan from (left) the C-band OU-PRIME and (right) the S-band KOUN both at 1856 UTC. The locations of OU-PRIME and KOUN are indicated with two white stars. The azimuthal direction of OU-PRIME's RHI scan (as in Fig. 2) is also included and denoted by a solid black line.

of the OU-PRIME RHI scan at a range of approximately 50–55 km at 1858:21 UTC.

b. Spectral polarimetry at 0° elevation angle

In this work, the OU-PRIME's RHI data at the lowest elevation angle (0°) were used to calculate spectral

polarimetry, where 960 complex-valued IQ samples were available for H and V channels at each gate. Specifically, at each range gate, 32 IQ samples for each channel were first zero padded to 64 points and then Fourier transformed using a Hanning window. The power spectral density (PSD) for each of the H and V channels as well

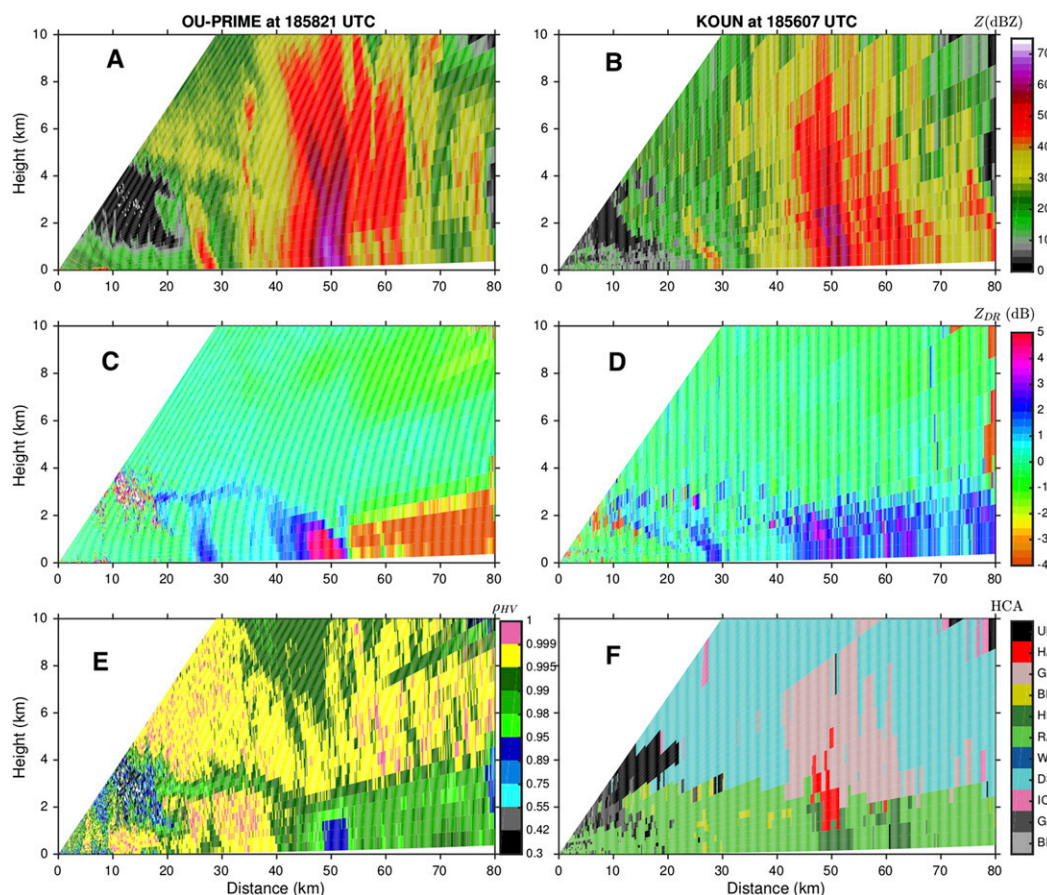


FIG. 2. The hailstorm observed by the RHI scan from (left) the C-band OU-PRIME at 1858 UTC and (right) the interpolated S-band KOUN at 1856 UTC.

as the cross-spectral density (CSD) between the two channels were computed. Note that PSD is also referred to as Doppler spectrum (Doviak and Zrnić 1993) or spectral reflectivity after calibration. Subsequently, 30 PSDs and CSDs were averaged to reduce the variance of the estimation (Yu et al. 2012). The averaged PSDs for H and V channels are denoted by S_H and S_V , and spectral differential reflectivity is calculated as $sZ_{DR} = S_H/S_V$.

Before the discussion of sZ_{DR} , the range profiles of Z , Z_{DR} , and ρ_{HV} along 233.3° between 43.75 and 58.625 km from C-band OU-PRIME at 1858:21 UTC at 0° elevation are shown in Fig. 3. The interpolated profiles from S-band KOUN at 1856:07 UTC are also included in Fig. 3 as references. Relatively larger Z and Z_{DR} and lower ρ_{HV} from C-band OU-PRIME than those from the S-band KOUN can be observed up to approximately 50 km, which suggests the resonance effect. Additionally, the attenuation and differential attenuation of OU-PRIME data, manifested by decreased reflectivity and differential reflectivity compared to

S-band data (Borowska et al. 2011), can be clearly observed after 52.5 km.

The Doppler spectrum from H channel (S_H) and sZ_{DR} from five selected locations, indicated by the upward arrows in Fig. 3, are shown in Fig. 4 from left to right. The range (in km), Z , and Z_{DR} are also included at each panel as references. Note that both S_H and sZ_{DR} were dealiased to be within -25.4 to 9.4 ms^{-1} for clearer presentation, based on the maximum unambiguous velocity of 17.7 ms^{-1} . Although spectral polarimetry has the potential for providing insights of hydrometeor properties within the radar resolution volume, one of the challenges is that it is difficult to decide which part of the spectra is reliable, owing to the high variance of those estimators. Yu et al. (2012) devised a spectral SNR threshold to meet a user-defined quality of the spectral estimators for a given spectral averaging. Since 30 gates averaged PSDs and CSDs are used in this work, the derived thresholds for the bias of sZ_{DR} , the standard deviation (SD) of sZ_{DR} , and the normalized spectral correlation coefficient were calculated as 0.04 dB, 0.707,

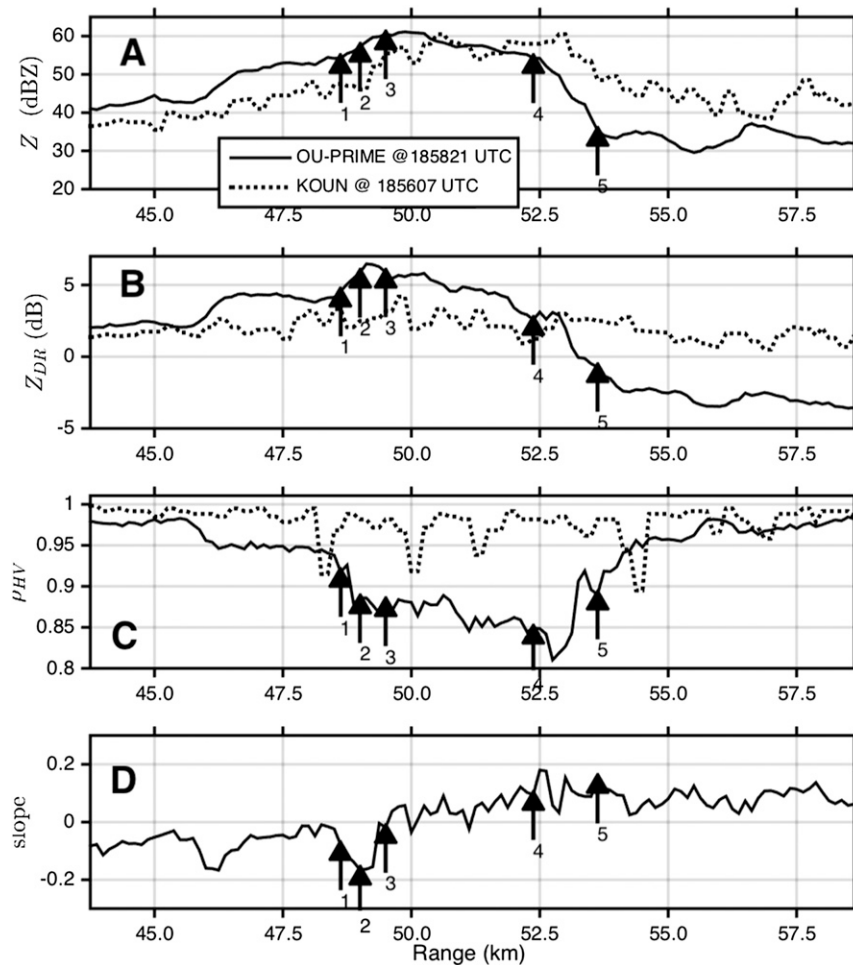


FIG. 3. The range profiles of (a) reflectivity, (b) differential reflectivity, (c) correlation coefficient, and (d) slope of spectral differential reflectivity at 1858:21 UTC. The interpolated reflectivity, differential reflectivity, and correlation coefficient from KOUN are included with dashed lines. The five selected locations for Doppler spectrum and spectral differential reflectivity shown in Fig. 4 are also labeled.

and 0.01, respectively (Yu et al. 2012). The portion of S_H and sZ_{DR} meeting those requirements are superimposed and denoted by thick lines. It is evident that the pattern of sZ_{DR} at different ranges exhibits interesting and distinct variations. To quantify the variations, a linear fitting was performed using only those sZ_{DR} that meet the quality requirements. The fitted lines are denoted by dashed lines in the sZ_{DR} plots and the value of slope [$\text{dB} (\text{m s}^{-1})^{-1}$] is also presented. The range profile of sZ_{DR} slope is also presented in Fig. 3d.

From Fig. 4, it is clear that the Doppler spectra are fairly wide with non-Gaussian shapes. It has been reported that similar broad and flattop spectra can be observed in strongly sheared environments (Yu et al. 2009). Additionally, turbulence can further broaden

the spectrum (Doviak and Zrnić 1993). The presence of vertical shear is inferred from the range profile of mean radial velocity from the two lowest elevations (0° and 0.5°) of OU-PRIME. Vertical shear of more than 0.02 s^{-1} in the negative radial direction (i.e., $< -0.02 \text{ s}^{-1}$, where negative direction is toward the radar) can be observed up to range of 48.5 km, where the height difference of the two lowest beams are approximately 423.2 m (Doviak and Zrnić 1993). Beyond the range of 48.5 km, an averaged shear of -0.01 s^{-1} is still obtained. The strong vertical shear was also verified by the observation from a mesonet station close to Rush Spring, which locates at $(-41.2, -53.9)$ km from OU-PRIME.

From Fig. 4, it can be observed that from location 1 to 2, the negative slope becomes steeper and both

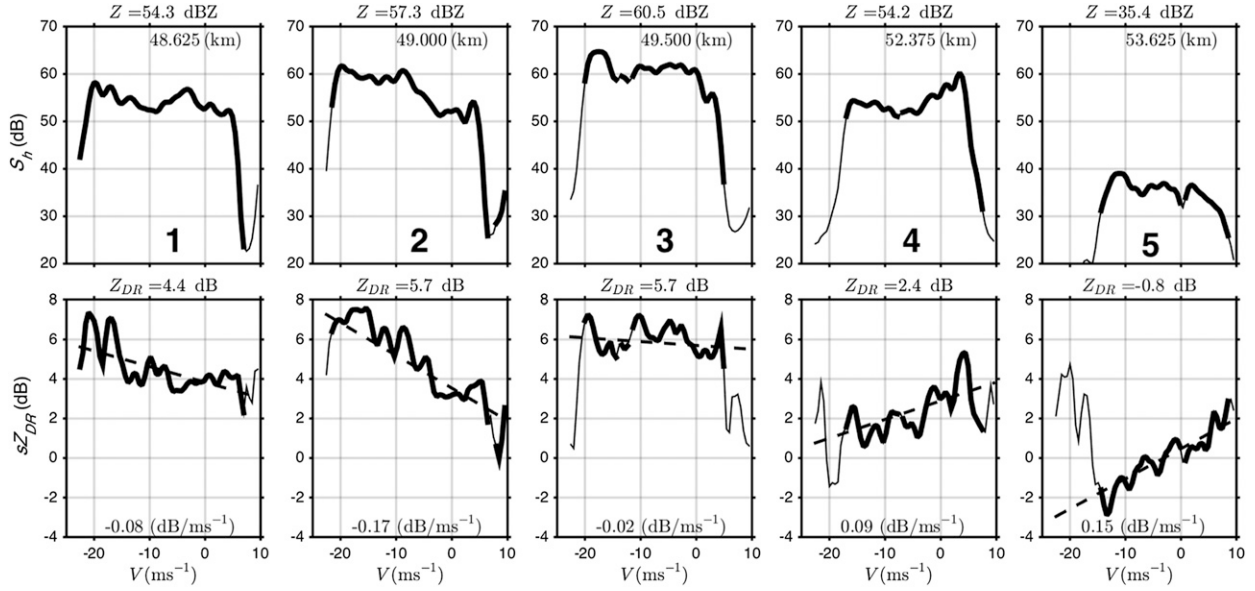


FIG. 4. (top) Doppler spectra and (bottom) spectral differential reflectivity from five specific locations indicated in Fig. 3. The data are from 0° elevation angle observed by OU-PRIME at 1858:21 UTC. The fitted lines are denoted by dashed lines in the sZ_{DR} plots and the value of the slope $[\text{dB} (\text{m s}^{-1})^{-1}]$ is also included.

Z and Z_{DR} increase. The largest negative slope of approximately $-0.17 \text{ dB} (\text{ms}^{-1})^{-1}$ and the maximum Z_{DR} value of 5.7 dB were obtained at location 2. At location 3, the sZ_{DR} becomes flattened with a slope of approximately zero, and both Z and Z_{DR} reach their maximum values of 60.5 dBZ and 5.7 dB , respectively. Though similar Z_{DR} values of approximately 5.7 dB are obtained at locations 2 and 3, distinctly different sZ_{DR} slopes are observed. This suggests the dynamic and/or microphysics in these two radar volumes are different, and spectral polarimetry has the potential to reveal it. Moreover, sZ_{DR} exhibits positive slope at locations 4 and 5, while sZ_{DR} values at location 5 are generally lower than those at location 4 for most of radial velocities. It is evident from Fig. 3 that the decreases of Z and Z_{DR} in location 5 are caused by attenuation and differential attenuation. Given the analysis presented so far, it is hypothesized that the observed variations of sZ_{DR} slope at 0° elevation angle is caused by shear-induced size sorting of a mixture of rain and melting hail in a turbulent environment. In section 4, this hypothesis will be tested, and the impacts of microphysical and dynamical characteristics on the sZ_{DR} will be studied using simulation.

3. A brief overview of shear-induced size sorting

The trajectory of hydrometeors in a sheared environment was first investigated in Marshall (1953). Pinsky and Khain (2006) also showed that the

approximated trajectory of a hydrometeor and its inclination are related to vertical shear. The equation of motion for falling hydrometeors in sheared environment was derived in many previous studies, such as Brussaard (1974, 1976), Bohne (1982), and Beard and Jameson (1983), and is briefly reviewed here. The primary forces on a single hydrometeor are the gravity force and drag force. In this work, only horizontal \mathbf{a}_h and vertical \mathbf{a}_z directions are considered, in which positive \mathbf{a}_z is upward. For a single hydrometeor of size D , when it falls through a sheared region, its velocity is $\mathbf{V} = \mathbf{a}_h V_h + \mathbf{a}_z V_z$. Initially, the hydrometeor is located at height H and its velocity is equal to the environment wind velocity at H , $\mathbf{U}(H) = \mathbf{a}_h U_h$, where only the horizontal air motion is considered. From Newton's second law, the net force \mathbf{F}_n on the hydrometeor is represented in the following equation:

$$\mathbf{F}_n = \mathbf{F}_g + \mathbf{F}_d, \quad (1)$$

where $\mathbf{F}_g = m\mathbf{g}$ is the gravity force, m is the mass, $\mathbf{g} = \mathbf{a}_h 0 + \mathbf{a}_z(-g)$, and g is the gravitational acceleration. The drag (or air resistance) force \mathbf{F}_d is obtained using the following equation (Bohne 1982):

$$\mathbf{F}_d = -m \frac{\mathbf{V} - \mathbf{U}}{\tau}, \quad (2)$$

where the time constant $\tau = V_t(D)/g$ and $V_t(D)$ is the terminal speed of a hydrometeor with size D .

The hydrometeor's horizontal and vertical velocities can be derived as

$$V_h(t) = U_h(t) + \frac{sV_t^2(D)}{g}, \quad (3a)$$

$$V_z(t) = -V_t(D), \quad (3b)$$

where $s = dU_h/dz$ is constant vertical shear. The canting angle of the hydrometeor (γ) in shear is also obtained as $\tan\gamma = -sV_t(D)/g$ (e.g., Brussaard 1974, 1976). The radar-observed radial velocity from the hydrometeor is the sum of the radial components from the two velocities as $v = V_h \cos\theta + V_z \sin\theta$, where θ is the elevation angle. For a higher elevation angle, the size sorting can be contributed from both horizontal and vertical components of the falling hydrometeors. However, for the elevation angle of 0° , the presence of size sorting is contributed only from the shear term in the horizontal component. For example, for a distribution of hydrometeors with sizes ranging between D_{\min} and D_{\max} in a sheared environment without turbulence and background wind [$U_h(t) = 0$], an interval of radial velocities from $sV_t^2(D_{\min})/g$ to $sV_t^2(D_{\max})/g$ results from 0° elevation angle, where D_{\min} and D_{\max} are the minimum and maximum sizes, respectively. As expected, no size sorting will be observed at 0° elevation angle if the shear is not present, and all the hydrometeors have the same radial velocity as the background wind. Note the sign of shear will determine the sign of radial velocity, where the convention of positive sign indicates outbound velocity. Additionally, the background wind of $U_h(t)$ will only shift the interval of radial velocity by the amount of $U_h(t)$.

4. Simulation

a. Description of simulation

To test the hypothesis and investigate the impacts of particle size distributions on Z , Z_{DR} , and the slope of sZ_{DR} , a numerical simulation was developed in the current work. Spek et al. (2008) developed a model of S-band Doppler spectrum and spectral differential reflectivity for a mixture of two types of ice particles with different particle size distribution functions. A similar model was also developed in the particle size distributions retrieval for a mixture of rain and melting hail in a turbulent environment (Wang 2010). In this work, the simulation used in Wang (2010) is extended to include both shear-induced size sorting and attenuation. The attenuated Doppler spectrum and spectral differential reflectivity can be generated from single or mixed types of hydrometeors in a turbulent and sheared environment.

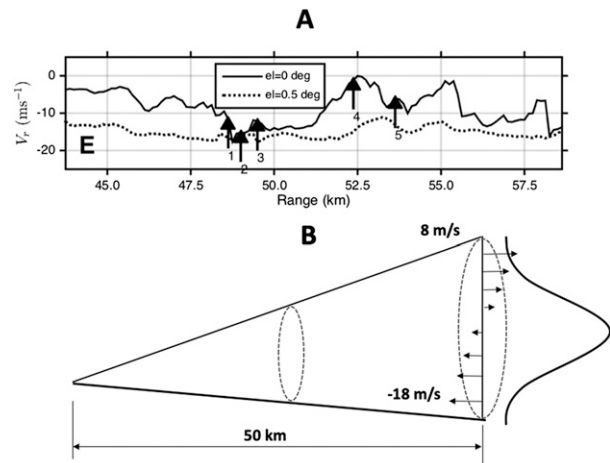


FIG. 5. (a) The profiles of OU-PRIME radial velocity from the elevation angles of 0° (solid line) and 0.5° (dashed line). (b) The simulated radar volume. The beamwidth is 0.5° , and the distance from this resolution volume to radar is 50 km. The background wind gradually changes from 18 m s^{-1} toward the radar at the bottom to 8 m s^{-1} forward from the radar at the top of the volume.

The method of simulating the sheared environment is demonstrated in Fig. 5b, where the distance from OU-PRIME to the radar gate of interest is 50 km as in the observation (Fig. 4). The Gaussian shape beam pattern is also included. As shown in Fig. 5a, the radial velocities at 0° and 0.5° elevation angles are -13 and -17 m s^{-1} at location 1, respectively. Since the maximum unambiguity velocity of OU-PRIME is 17.7 m s^{-1} , the dealiasing radial velocity can reach around 17 m s^{-1} at 0.5° elevation angle. Therefore, in the current work, the background wind at the bottom of the radar volume is set as 18 m s^{-1} toward to the radar, and gradually changes to 8 m s^{-1} forward from the radar at the top of the radar volume. Given the fact that OU-PRIME's beamwidth is half degree, the simulated vertical shear is approximately $s = -0.046 \text{ s}^{-1}$ at 50 km, and that is similar to the observation from a mesonet station close to Rush Spring. Within this sheared environment, particles from different heights within one radar resolution volume possess different background velocities, and their radial velocities are the combination of background wind and the velocities derived from section 3. Such strong vertical shear can generate a wide Doppler spectrum, as shown in Fig. 4.

A flowchart of the simulation is provided in Fig. 6, where the inputs and outputs are denoted by orange and green boxes, respectively. The input parameters include the particle size distributions from rain [$N_r(D_r)$] and from hail [$N_h(D_h)$], shear s , elevation angle θ , range r , and turbulence broadening σ_b . The idea is to first generate Doppler spectra for both H and V channels from individual hydrometeor type separately in a sheared

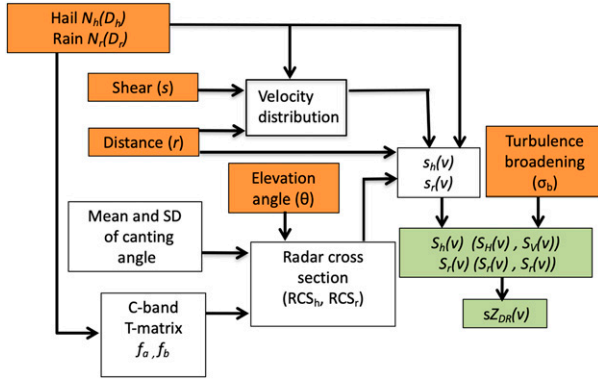


FIG. 6. Simulation flowchart. Input and output variables are denoted by orange and green boxes, respectively. Inputs are particle distribution of hail $[N_h(D_h)]$ and raindrops $[N_r(D_r)]$, vertical shear s , radar elevation angle θ , distance r , and turbulence broadening σ_b .

environment, and resulting Doppler spectra for H and V channels are the summations of individual spectra from each hydrometeor type. Subsequently, spectra are attenuated and further broadened by the turbulence.

In the current work, a gamma and an exponential distribution are used to simulate the particle distributions of raindrops and hailstones, respectively (e.g., Ulbrich 1983; Zhang et al. 2001):

$$N_r(D_r) = N_{r0} D_r^\mu e^{-\Lambda_r D_r}, \quad (4)$$

$$N_h(D_h) = N_{h0} e^{-\Lambda_h D_h}, \quad (5)$$

where the diameters of raindrops D_r and hailstones D_h are set as 0.1–8 and 8–25 mm, respectively. The intercept N_{h0} is $400\Lambda_h^{4.11} \text{ m}^{-3} \text{ mm}^{-1}$ as suggested by Ryzhkov et al. (2013). The relations between N_{r0} , μ , and Λ_r used in this work fit the results discussed by Zhang et al. (2001). The impacts of N_{r0} , N_{h0} , μ , Λ_r , and Λ_h on the simulated S_H and sZ_{DR} will be discussed in section 4b.

The C-band radar backscattering cross section for each size and hydrometeor type is calculated from the complex backscattering amplitudes $[f_a(\pi)]$ and $[f_b(\pi)]$ using the T-matrix code (Mishchenko 2000). The aspect ratio of raindrop as a function of its equivolume diameter (Brandes et al. 2002) and the dielectric constant of water at 20°C are inputs into the T-matrix code. The obtained size dependencies of differential reflectivity Z_{DR} of raindrops are shown in Fig. 7c, where the mean canting angle is 0°, and standard deviation of canting angle is 10°. It is evident that the maximum value of differential reflectivity resulting from resonance effects is 6.32 dB at $D_r = 5.4$ mm.

The hailstones in this work are modeled as uniform particles with various fractional water contents (spongy

hailstones) as defined by Ryzhkov et al. (2011). When hailstones start to melt, the mass water fractions vary with diameters and can be calculated with the model proposed by Rasmussen and Heymsfield (1987). As shown in Fig. 7b, if the hailstones with diameters less than 8 mm are assumed fully melted, the mass water fraction decreases with the increase of the hailstones' size, and it reaches 0.13 when the diameter is 25 mm. This is consistent with the simulation results from Ryzhkov et al. (2013). Dielectric constants of melting hailstones are determined by the dielectric constants of water, ice, air, and water volume fraction (Ryzhkov et al. 2011). The aspect ratio of melting hail is calculated using the model proposed by Rasmussen et al. (1984). The size dependencies of Z_{DR} of melting hail are also shown in Fig. 7d, where the mean canting angle is 0°. The standard deviations of canting angle are taken as a function of mass water content following (Ryzhkov et al. 2011):

$$\sigma = \sigma_s + f_{mw}(\sigma_r - \sigma_s), \quad (6)$$

where f_{mw} is the volume water fraction, and σ_r and σ_s are the standard deviations of canting angle distribution for raindrops and frozen hydrometeors (Ryzhkov et al. 2011). Note that using water-coated particles (i.e., with the two-layer T-matrix code) should produce more accurate simulation results, especially for very large ($D_h > 25$ mm) wet hail (Ryzhkov et al. 2011). However, since the maximum hail size is limited to 25 mm in this study, the uniform particles with Mishchenko (2000) T-matrix code can produce reasonable results.

With the obtained backscattering cross sections from raindrops and hailstones, the S_H and sZ_{DR} could be calculated with the spectral processing methods (e.g., Unal et al. 2001; Russchenberg et al. 2008; Yu et al. 2012). For an ideal case of maximum size sorting, where each radial velocity associated with each size can be fully resolved, sZ_{DR} from raindrop will have the same shape as in Fig. 7c. In practice, the shape of sZ_{DR} will be smoothed because velocity resolution is limited by dwell time and some amounts of turbulence are likely to occur. When a mixture of rain and melting hail occurs, the shape of sZ_{DR} is difficult to visualize intuitively, and will be determined from the amount of backscattered power at each velocity bin from the H and V channels. The unattenuated Doppler spectrum (H channel) from a hydrometeor of size D_i at velocity v can be obtained using the following equation (Spek et al. 2008):

$$S_H^{\text{un}}(v)dv = \sum_{i=1}^n N_i(D_i) \sigma_{HH,i} W(v), \quad (7)$$

where $i = r$ for rain and $i = h$ for hail, $N_i(D_i)$ is the particle size distribution defined in Eq. (4) or (5),

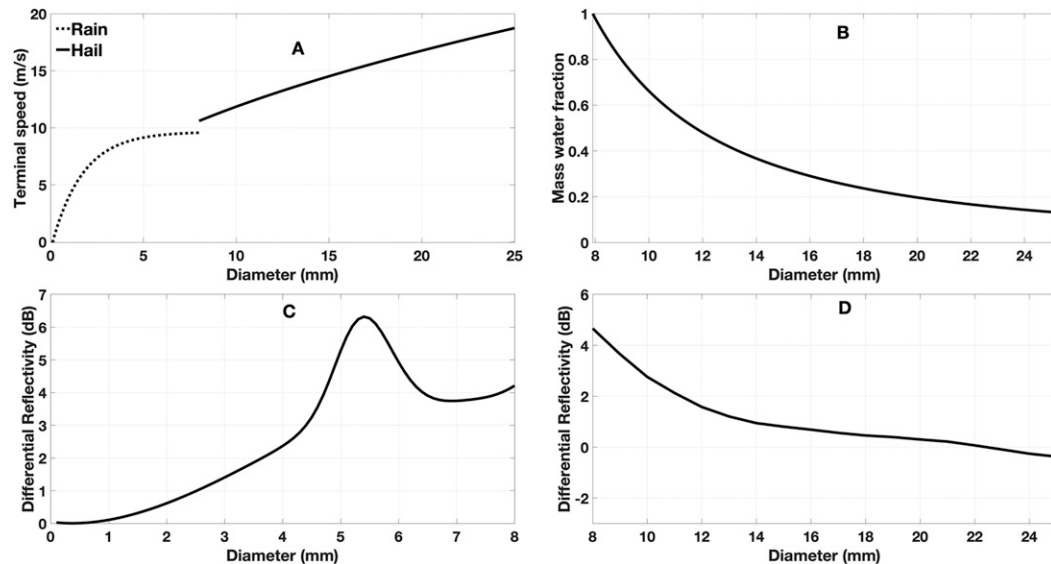


FIG. 7. (a) Terminal velocities of rain (dashed line) and hail (solid line) from different size. (b) The distribution of mass water fraction of melting hailstones along size. The hailstone with size less than 8 mm is assumed fully melted. (c) The differential reflectivity from raindrops with different sizes. The mean canting angle and the standard deviation are 0° and 10° , respectively. (d) The differential reflectivity from melting hailstones with different sizes. The mean canting angle is 0° , and the standard deviation is as a function of the water mass fraction.

$\sigma_{HH,i}$ ($\sigma_{VV,i}$) is the backscattering cross section from horizontal (vertical) direction, and $W(v)$ is the beam pattern at velocity v , as shown in Fig. 5. The superscript “un” means that the obtained Doppler spectrum is not attenuated.

After $S_H^{\text{un}}(v)$ is calculated using Eq. (7), attenuation effects are accounted for as

$$S_H(v) = S_H^{\text{un}}(v) - \mathbf{A}_h \times r, \quad (8)$$

where r is the distance, and A_h is specific attenuation (dB km^{-1}) at horizontal polarization, which is calculated as $A_h = 8.686 \times 10^{-3} \text{Im}(\langle f_a(0) \rangle)$. The variable $f_a(0)$ is the forward scattering amplitude at horizontal polarization and is calculated using the T-matrix method as described above, and $\langle f_a(0) \rangle$ is the average over the particle size distribution. Similarly, the attenuated Doppler spectrum for the V channel S_V could be calculated with $\langle f_b(0) \rangle$, and the attenuated sZ_{DR} can be therefore obtained. It should be noted that attenuation is a path and volume integrated, and the same attenuation is applied for all the particles in the same simulated radar volume. Therefore, the specific attenuation and specific differential attenuation will affect the obtained Z and Z_{DR} (Jameson 1992; Carey et al. 2000), but the effects on the shape of S_h and sZ_{DR} can be ignored.

The next step is to determine the relationship between the drop size and radial velocity; therefore, the

dependence of Doppler spectrum on drop size can be converted onto radial velocity as in Eq. (7). Specifically, the radial velocity for each size of hydrometeor in a sheared environment is determined by the background wind (Fig. 5b) and its shear-induced radial velocity obtained from Eqs. (3a) and (3b) at an elevation angle of θ . In this work, the terminal velocity for raindrops and hail (Fig. 7a) is determined by using the formula in Atlas et al. (1973) and Mitchell (1996), respectively. The spectra for each hydrometeor types and polarization are then broadened by turbulence by convolving with a Gaussian kernel of width σ_b (e.g., Spek et al. 2008). The resulting Doppler spectrum for the H channel S_H is the sum of the broadened spectra from rain and melting hail for the H channel.

b. Simulation results

1) CASE I: RAIN ONLY

In this case, Doppler spectrum and spectral differential reflectivity are simulated with raindrops only, and the simulated results are shown in Figs. 8 and 9, respectively. Because of the size sorting, particle size distribution shows clear vertical variations in one radar resolution volume, and these variations are simulated through changing coefficients of N_{r0} , μ , and Λ_r in Eq. (4). In Fig. 8, from the top to the bottom of the resolution volume, N_{r0} (Λ_r) gradually changes

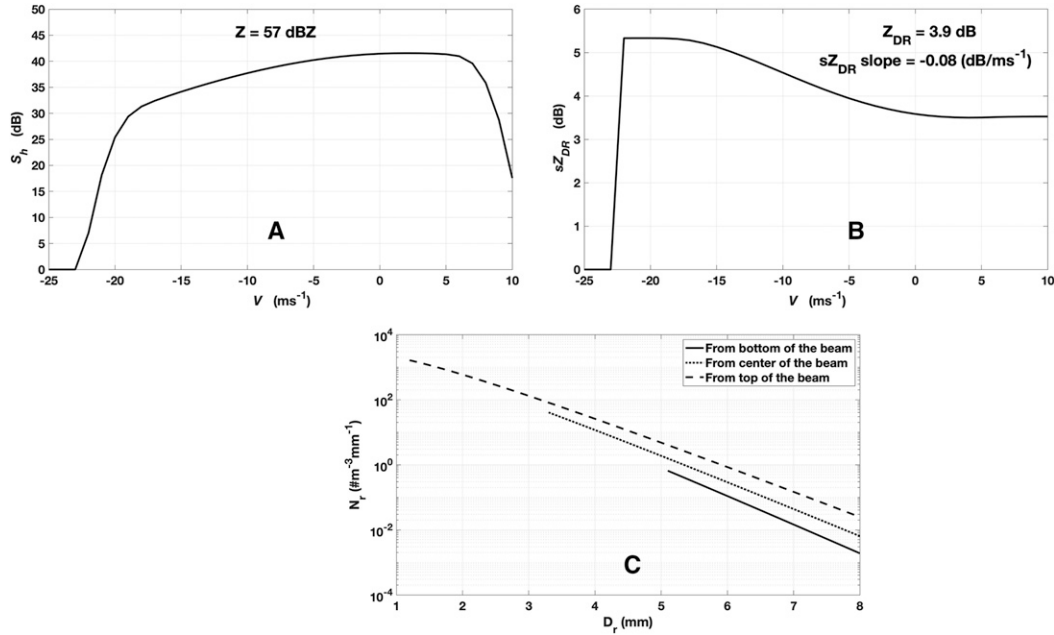


FIG. 8. (a) Simulated Doppler spectrum, (b) spectral differential reflectivity, and (c) particle size distribution of raindrop. Only raindrops are used in this case; details about the particle size distribution can be found in text. Examples of particle size distributions from top, center, and bottom in the resolution volume are presented with solid, dotted, and dashed lines, respectively. The obtained Doppler spectrum, spectral differential reflectivity, slope of sZ_{DR} , reflectivity, and differential reflectivity are similar to the observations from location 1.

from $13\,000 \text{ m}^{-3} \text{mm}^{-1}$ (1.9 mm^{-1}) to $8000 \text{ m}^{-3} \text{mm}^{-1}$ (2.7 mm^{-1}), and the value of μ is set as 1 in all the altitudes. All these values are within the reasonable ranges as indicated by Zhang et al. (2001). Examples of N_r from top, center, and bottom of the radar resolution volume are shown in Fig. 8c with solid, dotted, and dashed lines, respectively. Because of the size sorting, the amount of small drops shows decreasing trend from the top to the bottom in the resolution volume, and small size raindrops are gradually absent when they fall down (Kumjian and Ryzhkov 2012). Therefore, raindrops with all sizes (from 1 to 8 mm) could be found from the top of the resolution volume, but only big drops could be found from the bottom of the resolution volume. In this work, we assume raindrops with diameter smaller than 5.1 mm are totally absent at the bottom of the resolution volume. The simulated S_h and sZ_{DR} are shown in Figs. 8a and 8b, the obtained Z , Z_{DR} , and slope of sZ_{DR} are 57 dBZ, 3.9 dB, and $-0.08 \text{ dB (ms}^{-1}\text{)}^{-1}$, respectively. These values are close to the observations from location 1.

Following the same procedure, the observed Doppler spectrum and spectral differential reflectivity from location 2 are simulated, and the results are shown in Figs. 9a and 9b. Different from location 1, a smaller amount of small drops are used in the simulation, but

more large drops are added as shown in Fig. 9c. These large raindrops mainly come from the shedding process of melting hailstones (Ryzhkov et al. 2013). From the top of the resolution volume to the bottom, the values of μ gradually increase from -1.9 to 3.5 , and the setting for N_{r0} and Λ_r are the same as in location 1. The obtained Z , Z_{DR} , and slope of sZ_{DR} are 57 dBZ, 4.8 dB, and $-0.16 \text{ dB (ms}^{-1}\text{)}^{-1}$. Comparing the results from locations 1 and 2, although they show similar Z and Z_{DR} , significantly different slopes of sZ_{DR} can be found. It should be noted, in the observation, the sZ_{DR} can reach approximate 8 dB at velocity bin of -18 ms^{-1} , but the maximum value as simulation is around 5.12 dB. These large sZ_{DR} bins may come from big drops from fully or partially melted hail. Because the aspect ratio for such large drops or small melting hailstones are still under investigation (Thurai et al. 2013; Kumjian et al. 2018), we did not add such big drops in the simulation. As a result of lacking such big drops, the simulated Z_{DR} is 4.8 dB, which is smaller than the observed 5.7 dB.

2) CASE II: MIXTURE OF RAIN AND MELTING HAIL

In this case, a mixture of rain and melting hail is investigated, and results are shown in Figs. 10 and 11. Two scenarios are simulated with different amounts of hail, and the particle size distributions of rain are the

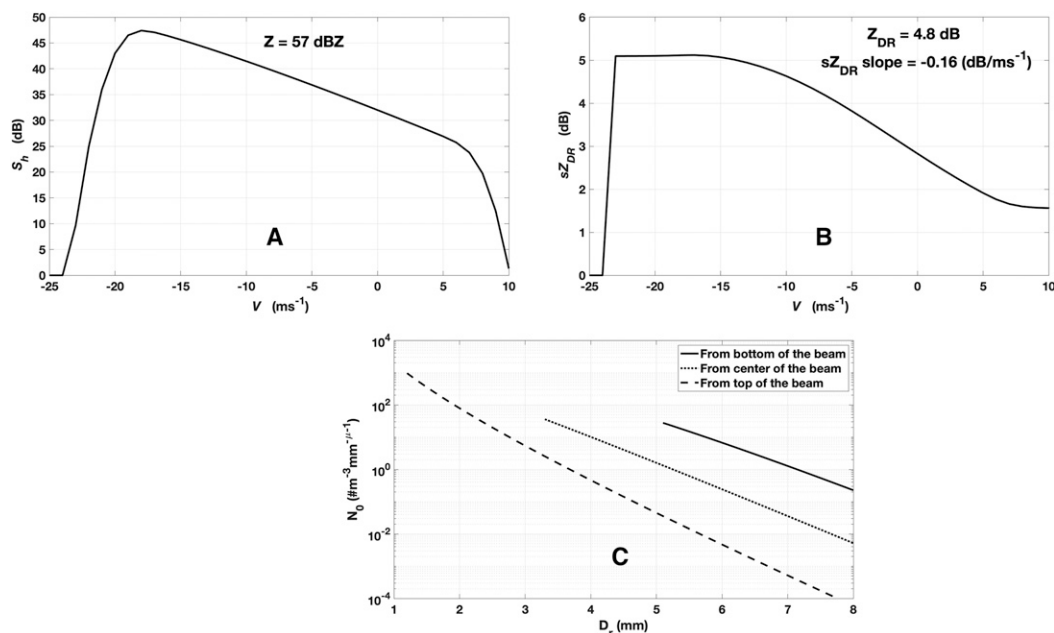


FIG. 9. As in Fig. 8, but the obtained Doppler spectrum, spectral differential reflectivity, slope of sZ_{DR} , reflectivity, and differential reflectivity are similar to the observations from location 2.

same. From the top to the bottom of the resolution volume, N_{r0} (A) gradually changes from $13000 \text{ m}^{-3} \text{ mm}^{-1}$ (1.9 mm^{-1}) to $8000 \text{ m}^{-3} \text{ mm}^{-1}$ (2.7 mm^{-1}) as in Fig. 10c, and the value of μ is set as 2 in all the altitudes. This particle size distribution of rain is applied to both scenarios. In Fig. 10d, N_{h0} is set as $400 \text{ m}^{-3} \text{ mm}^{-1}$, and Λ_h is set as 1.14 mm^{-1} from all the altitudes in the resolution volume; the obtained Z , Z_{DR} , and slope of sZ_{DR} are 60 dBZ , 4.2 dB , and $-0.02 \text{ dB (ms}^{-1})^{-1}$. The simulated Doppler spectrum and spectral differential reflectivity are shown in Figs. 10a and 10b, and they show similar features as the observations from location 3 in Fig. 4. It should be noted that the Z and Z_{DR} values from locations 1, 2, and 3 show similar values, but the slopes of sZ_{DR} show significantly different values. In these three locations, significant changes in the particle size distribution and hydrometeor species are simulated, but the integrated Z and Z_{DR} values are not sensitive to these changes. Therefore, the slope of sZ_{DR} could be used as an indicator of variations in the particle size distribution and classes.

In Fig. 11, from the top to the bottom of the resolution volume, Λ_h gradually changes from 0.84 to 0.3 mm^{-1} , and N_{h0} is set as $400 \text{ m}^{-3} \text{ mm}^{-1}$. Examples of N_h from top, center, and bottom of the radar resolution volume are shown in Fig. 11c with solid, dotted, and dashed lines, respectively. For the given particle size distributions of rain and hail, the obtained sZ_{DR} shows

positive slope of $0.09 \text{ dB (ms}^{-1})^{-1}$, which is similar to the observation from location 4. From location 2 to location 4, Z and Z_{DR} show similar values, but the slope of sZ_{DR} changes from negative to positive. With the same background wind environment, the changes in the sZ_{DR} slope are simulated through adjusting the particle size distributions. The observed Z and Z_{DR} is higher than simulation because of the attenuation, and the attenuation effect is more obvious in location 5.

3) CASE III: RAIN ONLY FROM A REGION WITHOUT VERTICAL SHEAR

The Doppler spectrum and the spectral differential reflectivity from regions away from the strong vertical shear were also examined and simulated in the current work. Three continuous locations (azimuthal angle: 240° ; ranges: 44.375 , 44.5 , and 44.625 km) were selected because 1) they are away from the shear region, and 2) they are associated with large signal-to-noise ratio. The S_H (Figs. 12a–c) and sZ_{DR} (Figs. 12d–f) are shown in Fig. 12. The linearly fitted sZ_{DR} is also shown in Figs. 12d–f with a dashed line. It should be noted that only the high signal-to-noise ratio (SNR) portion with $S_H(v) > 10 \text{ dB}$ (thick solid line) is used in the fitting, and the low $S_H(v)$ portion (thin dashed line) is not used in the fitting because they are associated with large fluctuation caused by low SNR. It could be found that the S_H exhibits a Gaussian-shaped spectrum, and the sZ_{DR} shows a flat-top-shape signature. Because there is no

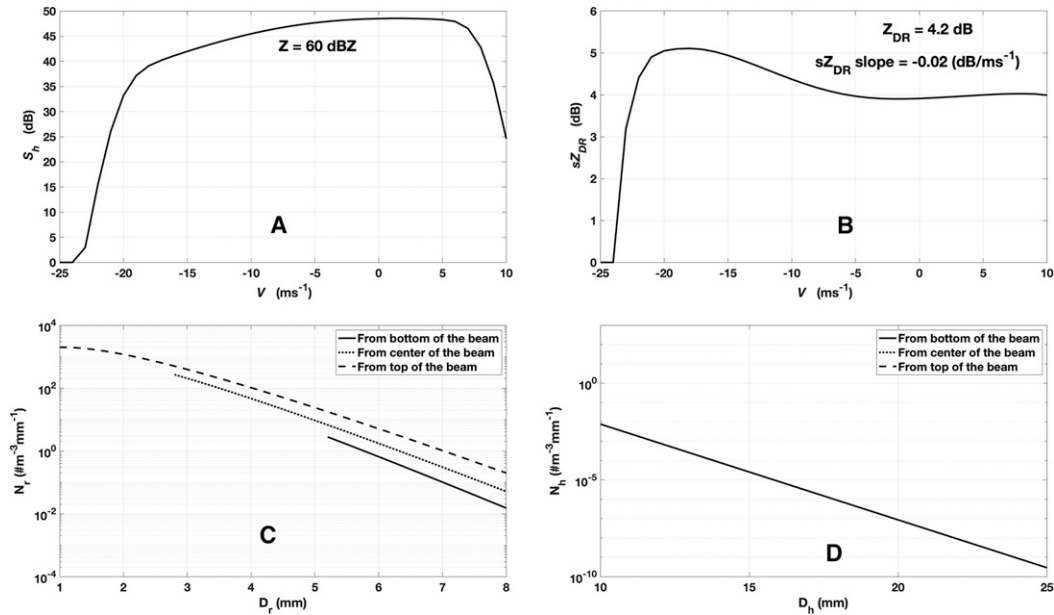


FIG. 10. (a) Simulated Doppler spectrum, (b) spectral differential reflectivity, (c) particle size distribution of raindrop, and (d) particle size distribution of hail. Details about the particle size distribution can be found in text. The obtained Doppler spectrum, spectral differential reflectivity, slope of sZ_{DR} , reflectivity, and differential reflectivity are similar to the observations from location 3.

strong vertical shear, both S_H and sZ_{DR} are associated with small spectral width.

The simulated Doppler spectrum and the spectral differential reflectivity are presented in Fig. 13. Because there is no size sorting caused by strong vertical shear, a

uniform particle size distribution is used in the whole simulation volume with the following settings: $N_{r0} = 9000 \text{ m}^{-3} \text{ mm}^{-1}$, $\mu = 1$, and $\Lambda_r = 2 \text{ mm}^{-1}$. Because this region is away from the hail region, there are no hailstones added in the simulation. The background wind is

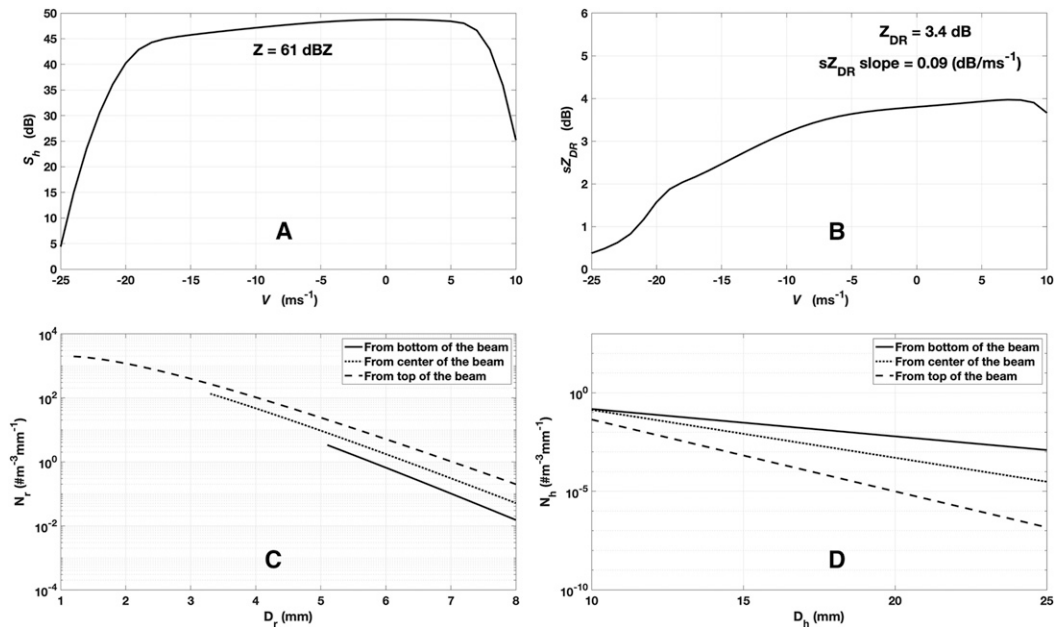


FIG. 11. As in Fig. 10, but the obtained Doppler spectrum, spectral differential reflectivity, slope of sZ_{DR} , reflectivity, and differential reflectivity are similar to the observations from location 4.

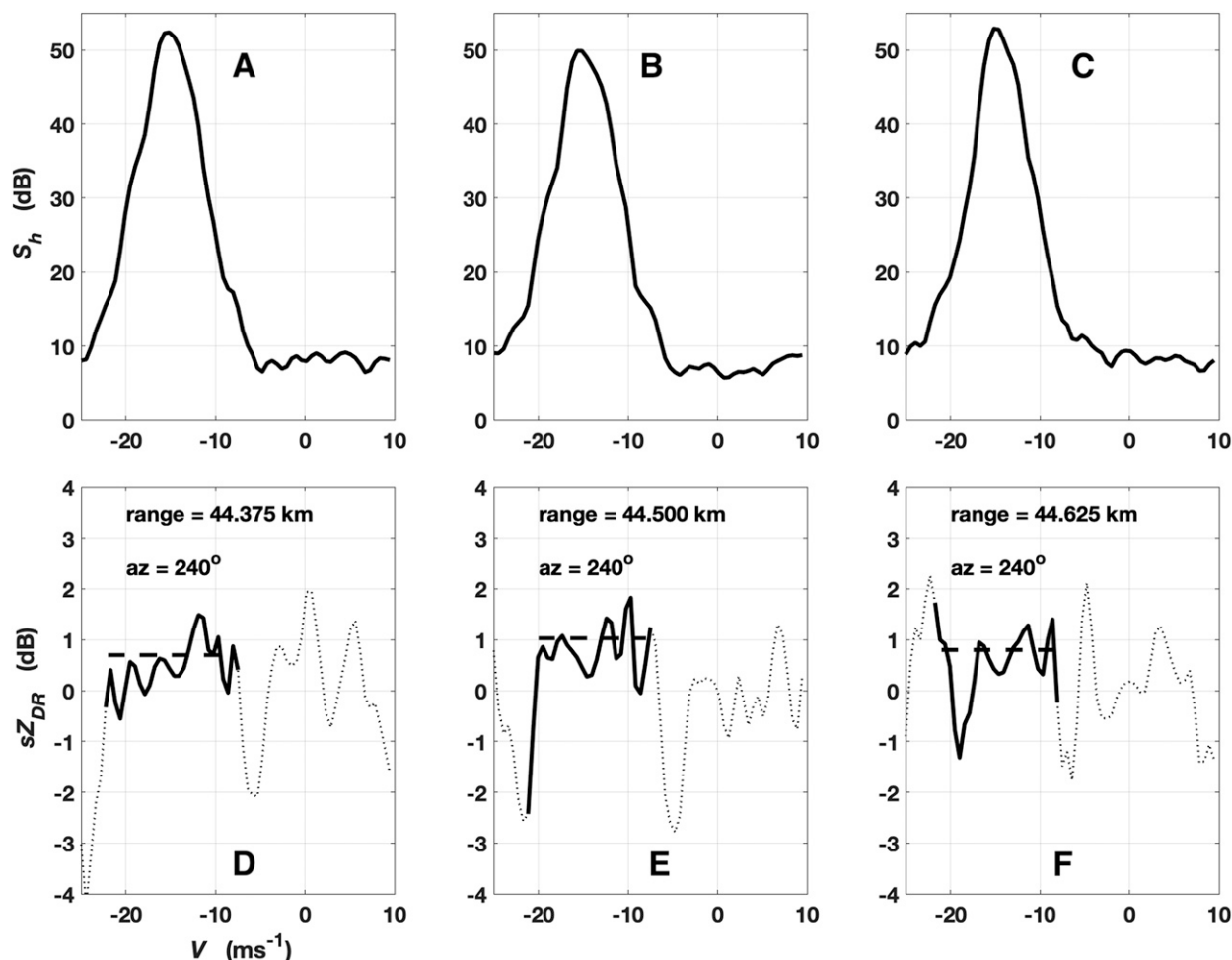


FIG. 12. (a)–(c) Doppler spectrum and (d)–(f) spectral differential reflectivity observed from three locations away from the shear region. The azimuthal angle of these locations is 240° , and ranges are 44.375, 44.5, and 44.625 km. The linearly fitted results are also included as dashed lines.

set as -15 m s^{-1} , and there is no vertical shear applied. We found that Gaussian-shaped S_H with small spectral width and flattop-shaped sZ_{DR} were obtained, and these results are consistent with the observations shown in Fig. 12.

5. Summary and conclusions

Spectral polarimetry links the Doppler and polarimetric information within the radar resolution volume through spectral processing. For example, Doppler spectrum and spectral differential reflectivity represent distributions of reflectivity and differential reflectivity as a function of radial velocity. In the past, spectral polarimetry has been applied to observations at higher elevations where the size sorting of hydrometeors is dominated by their size-dependent terminal velocities. In this work, spectral polarimetry was applied to observations of a hailstorm at 0° elevation angle with the

C-band OU-PRIME. Broad and flattop spectra were observed and the spectral differential reflectivity exhibited interesting and distinct variation of slopes at different ranges. It is hypothesized that those observed features in spectra of reflectivity and differential reflectivity are caused by shear-induced size sorting of a mixture of rain and melting hail in a turbulent environment. Additionally, the profiles of mean radial velocities from the lowest two elevations and mesonet wind data further support the presence of strong vertical shear. By comparing the polarimetric variables from the C-band OU-PRIME and the nearby S-band KOUN, the resonance effects at C band caused by large raindrops and melting hail are evident, which is manifested by enhanced reflectivity and differential reflectivity and decreased correlation coefficient.

Numerical simulations were carried out to study the impact of various microphysical and dynamical variables on the slope of spectral differential reflectivity.

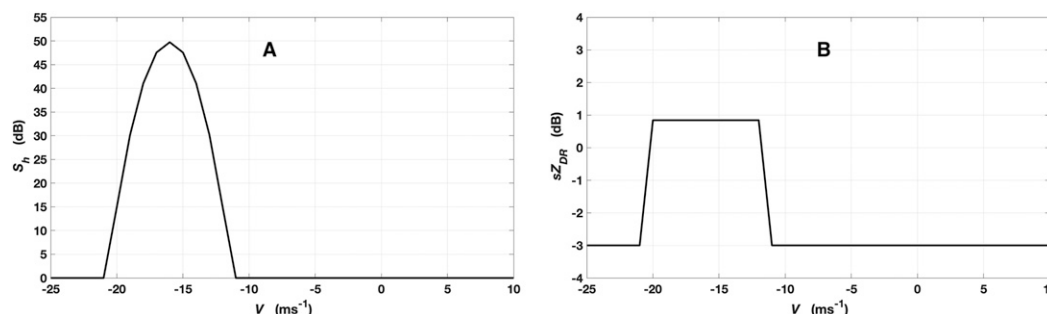


FIG. 13. As in Fig. 10, but for (a) the obtained Doppler spectrum, and (b) spectral differential reflectivity according to the observations from Fig. 12.

In this work, Doppler spectrum and spectral differential reflectivity from four distinct locations are simulated using different particle size distributions and hydrometeor species in a sheared environment. The reflectivity and differential reflectivity from these four locations show similar values, but the slopes of spectral differential reflectivity show significantly different values. Through adjusting the particle size distributions within a reasonable range, the observations from these four locations could be regenerated. It should be noted that only one set of particle size distributions are used to simulate the Doppler spectrum and spectral differential reflectivity for each scenario in the current work. Other sets of particle size distribution should be able to generate similar results, and we do not enumerate all of them.

One of the limitations in spectral polarimetry for operational application is the requirement of spectral averaging. For example, 30 spectra were averaged in this work to reduce the statistical fluctuations in the spectral polarimetric variables. Even though spectral averaging can also be achieved in range, azimuthal, and frequency domain, the resolution in those domains is compromised. Fortunately, a resampling technique based on bootstrapping was recently developed to tackle this limitation to improve the quality of spectral polarimetric variables with relatively small number of samples (Umeyama 2016). It is envisioned that spectral polarimetry can be applied to other types of scenarios. For example, the study of tornado debris is one of them, where polarimetric signatures of debris are evident and centrifugal force can provide the size sorting. In this work, we focused on only one of the spectral polarimetric variables, spectral differential reflectivity, at the lowest elevation. Two other variables of spectral correlation coefficient and spectral differential phase can provide different aspects of microphysical properties. Studies on these two variables will be reported in subsequent work.

Acknowledgments. Matthew R. Kumjian was funded by NSF Award AGS-1661679 and by an award from the Insurance Institute for Business and Home Safety (IBHS). The authors thank Dr. Guifu Zhang for helpful discussion of the simulation, especially the implementation of attenuation.

REFERENCES

- Anderson, M. E., L. D. Carey, W. A. Petersen, and K. R. Knupp, 2011: C-band dual-polarimetric radar signatures of hail. *Electron. J. Oper. Meteor.*, 2011-EJ02, <http://nwafiles.nwas.org/ej/pdf/2011-EJ2.pdf>.
- Atlas, D., R. C. Srivastava, and R. S. Sekhon, 1973: Doppler radar characteristics of precipitation at vertical incidence. *Rev. Geophys. Space Phys.*, **11**, 1–35, <https://doi.org/10.1029/RG011i001p00001>.
- Beard, K. V., and A. R. Jameson, 1983: Raindrop canting. *J. Atmos. Sci.*, **40**, 448–453, [https://doi.org/10.1175/1520-0469\(1983\)040<0448:RC>2.0.CO;2](https://doi.org/10.1175/1520-0469(1983)040<0448:RC>2.0.CO;2).
- Bodine, D., R. D. Palmer, and G. Zhang, 2014: Dual-wavelength polarimetric radar analyses of tornadic debris signatures. *J. Appl. Meteor. Climatol.*, **53**, 242–261, <https://doi.org/10.1175/JAMC-D-13-0189.1>.
- Bohne, A. R., 1982: Radar detection of turbulence in precipitation environments. *J. Atmos. Sci.*, **39**, 1819–1837, [https://doi.org/10.1175/1520-0469\(1982\)039<1819:RDOTIP>2.0.CO;2](https://doi.org/10.1175/1520-0469(1982)039<1819:RDOTIP>2.0.CO;2).
- Borowska, L., A. V. Ryzhkov, and D. S. Zrnić, 2011: Attenuation and differential attenuation of 5-cm-wavelength radiation in melting hail. *J. Appl. Meteor. Climatol.*, **50**, 59–76, <https://doi.org/10.1175/2010JAMC2465.1>.
- Brandes, E. A., G. Zhang, and J. Vivekanandan, 2002: Experiments in rainfall estimation with a polarimetric radar in a subtropical environment. *J. Appl. Meteor.*, **41**, 674–685, [https://doi.org/10.1175/1520-0450\(2002\)041<0674:EIREWA>2.0.CO;2](https://doi.org/10.1175/1520-0450(2002)041<0674:EIREWA>2.0.CO;2); Corrigendum, **44**, 186, [https://doi.org/10.1175/1520-0450\(2005\)44<186:C>2.0.CO;2](https://doi.org/10.1175/1520-0450(2005)44<186:C>2.0.CO;2).
- Brussaard, G., 1974: Rain-induced cross polarization and raindrop canting. *Electron. Lett.*, **10**, 411–412.
- , 1976: A meteorological model for rain-induced cross polarization. *IEEE Trans. Antennas Propag.*, **24**, 5–11, <https://doi.org/10.1109/TAP.1976.1141282>.
- Carey, L. D., S. A. Rutledge, D. A. Ahijevych, and T. D. Keenan, 2000: Correcting propagation effects in C-band polarimetric radar observations of tropical convection using differential propagation phase. *J. Appl. Meteor.*, **39**, 1405–1433, [https://doi.org/10.1175/1520-0450\(2000\)039<1405:CPEICB>2.0.CO;2](https://doi.org/10.1175/1520-0450(2000)039<1405:CPEICB>2.0.CO;2).

- Chandrasekar, V., R. Keranen, S. Lim, and D. Moiseev, 2013: Recent advances in classification observations from dual polarization weather radars. *Atmos. Res.*, **119**, 97–111, <https://doi.org/10.1016/j.atmosres.2011.08.014>.
- Dawson, D. T., E. R. Mansell, Y. Jung, L. J. Wicker, M. R. Kumjian, and M. Xue, 2014: Low-level Z_{DR} signatures in supercell forward flanks: The role of size sorting and melting of hail. *J. Atmos. Sci.*, **71**, 276–299, <https://doi.org/10.1175/JAS-D-13-0118.1>.
- , —, and M. R. Kumjian, 2015: Does wind shear cause hydrometeor size sorting? *J. Atmos. Sci.*, **72**, 340–348, <https://doi.org/10.1175/JAS-D-14-0084.1>.
- Doviak, R. J., and D. S. Zrnić, 1993: *Doppler Radar and Weather Observations*. Academic Press, 562 pp.
- Hwang, Y., T.-Y. You, V. Lakshmanan, D. M. Kingfield, D.-I. Lee, and C.-H. You, 2017: Neuro-fuzzy gust front detection algorithm with S-band polarimetric radar. *IEEE Trans. Geosci. Remote Sens.*, **55**, 1618–1628, <https://doi.org/10.1109/TGRS.2016.2628520>.
- Jameson, A. R., 1992: The effect of temperature on attenuation correction schemes in rain using polarization propagation differential phase shift. *J. Appl. Meteor.*, **31**, 1106–1118, [https://doi.org/10.1175/1520-0450\(1992\)031<1106:TEOTOA>2.0.CO;2](https://doi.org/10.1175/1520-0450(1992)031<1106:TEOTOA>2.0.CO;2).
- Kumjian, M. R., 2013a: Principles and applications of dual-polarization weather radar. Part II: Warm- and cold-season applications. *J. Oper. Meteor.*, **1**, 243–264, <https://doi.org/10.1519/nwajom.2013.0120>.
- , 2013b: Principles and applications of dual-polarization weather radar. Part III: Artifacts. *J. Oper. Meteor.*, **1**, 265–274, <https://doi.org/10.1519/nwajom.2013.0121>.
- , and A. V. Ryzhkov, 2008: Polarimetric signatures in supercell thunderstorms. *J. Appl. Meteor. Climatol.*, **47**, 1940–1961, <https://doi.org/10.1175/2007JAMC1874.1>.
- , and —, 2009: Storm-relative helicity revealed from polarimetric radar measurements. *J. Atmos. Sci.*, **66**, 667–685, <https://doi.org/10.1175/2008JAS2815.1>.
- , and —, 2012: The impact of size sorting on the polarimetric radar variables. *J. Atmos. Sci.*, **69**, 2042–2060, <https://doi.org/10.1175/JAS-D-11-0125.1>.
- , Y. P. Richardson, T. Meyer, K. A. Kosiba, and J. Wurman, 2018: Resonance scattering effects in wet hail observed with the dual-X-band-frequency, dual-polarization Doppler on Wheels radar. *J. Appl. Meteor. Climatol.*, **57**, 2713–2731, <https://doi.org/10.1175/JAMC-D-17-0362.1>.
- Marshall, J. S., 1953: Precipitation trajectories and patterns. *J. Meteor.*, **10**, 25–29, [https://doi.org/10.1175/1520-0469\(1953\)010<0025:PTAP>2.0.CO;2](https://doi.org/10.1175/1520-0469(1953)010<0025:PTAP>2.0.CO;2).
- Meischner, P., Ed., 2003: *Weather Radar: Principles and Advanced Applications*. Springer, 337 pp.
- , V. N. Bringi, D. Heimann, and H. Holler, 1991: A squall line in southern Germany: Kinematics and precipitation formation as deduced by advanced polarimetric and Doppler radar measurements. *Mon. Wea. Rev.*, **119**, 678–701, [https://doi.org/10.1175/1520-0493\(1991\)119<0678:ASLISG>2.0.CO;2](https://doi.org/10.1175/1520-0493(1991)119<0678:ASLISG>2.0.CO;2).
- Mishchenko, M. I., 2000: Calculation of the amplitude matrix for a nonspherical particle in a fixed orientation. *Appl. Opt.*, **39**, 1026–1031, <https://doi.org/10.1364/AO.39.001026>.
- Mitchell, D. L., 1996: Use of mass- and area-dimensional power laws for determining precipitation particle terminal velocity. *J. Atmos. Sci.*, **53**, 1710–1723, [https://doi.org/10.1175/1520-0469\(1996\)053<1710:UOMAAD>2.0.CO;2](https://doi.org/10.1175/1520-0469(1996)053<1710:UOMAAD>2.0.CO;2).
- Moiseev, D. N., V. Chandrasekar, C. M. H. Unal, and H. W. J. Russchenberg, 2006: Dual-polarization spectral analysis for retrieval of effective raindrop shapes. *J. Atmos. Oceanic Technol.*, **23**, 1682–1695, <https://doi.org/10.1175/JTECH1945.1>.
- Palmer, R. D., and Coauthors, 2011: Observations of the 10 May 2010 tornado outbreak using OU-PRIME: Potential for new science with high-resolution polarimetric radar. *Bull. Amer. Meteor. Soc.*, **92**, 871–891, <https://doi.org/10.1175/2011BAMS3125.1>.
- Park, H., A. V. Ryzhkov, D. S. Zrnić, and K.-E. Kim, 2009: The hydrometeor classification algorithm for the polarimetric WSR-88D: Description and application to an MCS. *Wea. Forecasting*, **24**, 730–748, <https://doi.org/10.1175/2008WAF2222205.1>.
- Picca, J., and A. V. Ryzhkov, 2012: A dual-wavelength polarimetric analysis of the 16 May 2010 Oklahoma City extreme hailstorm. *Mon. Wea. Rev.*, **140**, 1385–1403, <https://doi.org/10.1175/MWR-D-11-00112.1>.
- Pinsky, M. B., and A. P. Khain, 2006: Initiation of drop velocity oscillations during their fall in a vertically sheared flow with embedded velocity fluctuation. *Geophys. Astrophys. Fluid Dyn.*, **78**, 169–192, <https://doi.org/10.1080/03091929408226577>.
- Rasmussen, R. M., and A. Heymsfield, 1987: Melting and shedding of graupel and hail. Part I: Model physics. *J. Atmos. Sci.*, **44**, 2754–2763, [https://doi.org/10.1175/1520-0469\(1987\)044<2754:MASOGA>2.0.CO;2](https://doi.org/10.1175/1520-0469(1987)044<2754:MASOGA>2.0.CO;2).
- , V. Levizzani, and H. R. Pruppacher, 1984: A wind tunnel study on the melting behavior of atmospheric ice particles. III: Experiment and theory for spherical ice particles of radius > 500 μm . *J. Atmos. Sci.*, **41**, 381–388, [https://doi.org/10.1175/1520-0469\(1984\)041<0381:AWTATS>2.0.CO;2](https://doi.org/10.1175/1520-0469(1984)041<0381:AWTATS>2.0.CO;2).
- Russchenberg, H., L. Spek, D. Moiseev, C. Unal, Y. Dufournet, and V. Chandrasekar, 2008: On the use of spectral polarimetry to observe ice cloud microphysics with radar. *Precipitation: Advances in Measurement, Estimation and Prediction*, Springer, 285–312.
- Ryzhkov, A. V., T. J. Schuur, D. W. Burgess, S. Giangrande, and D. S. Zrnić, 2005: The Joint Polarization Experiment: Polarimetric rainfall measurements and hydrometeor classification. *Bull. Amer. Meteor. Soc.*, **86**, 809–824, <https://doi.org/10.1175/BAMS-86-6-809>.
- , D. S. Zrnić, P. Zhang, J. Krause, H. S. Park, D. Hudak, J. Young, and J. L. Alford, 2007: Comparison of polarimetric algorithms for hydrometeor classification at S and C bands. *33rd Conf. on Radar Meteorology*, Cairns, Australia, Amer. Meteor. Soc., 10.3, https://ams.confex.com/ams/33Radar/techprogram/paper_123109.htm.
- , M. Pinsky, A. Pokrovsky, and A. Khain, 2011: Polarimetric radar observations operator for a cloud model with spectral microphysics. *J. Appl. Meteor. Climatol.*, **50**, 873–894, <https://doi.org/10.1175/2010JAMC2363.1>.
- , M. R. Kumjian, S. M. Ganson, and A. P. Khain, 2013: Polarimetric radar characteristics of melting hail. Part I: Theoretical simulations using spectral microphysical modeling. *J. Appl. Meteor. Climatol.*, **52**, 2849–2870, <https://doi.org/10.1175/JAMC-D-13-073.1>.
- Scharfenberg, K. A., and Coauthors, 2005: The Joint Polarization Experiment: Polarimetric radar in forecasting and warning decision making. *Wea. Forecasting*, **20**, 775–788, <https://doi.org/10.1175/WAF881.1>.
- Spek, A. L. J., C. M. H. Unal, D. N. Moiseev, H. W. J. Russchenberg, V. Chandrasekar, and Y. Dufournet, 2008: New technique to categorize and retrieve the microphysical properties of ice particles above the melting layer using radar dual-polarization spectral analysis. *J. Atmos. Oceanic Technol.*, **25**, 482–497, <https://doi.org/10.1175/2007JTECHA944.1>.
- Thurai, M., V. N. Bringi, W. A. Petersen, and P. N. Gatlin, 2013: Drop shapes and fall speeds in rain: Two contrasting

- examples. *J. Appl. Meteor. Climatol.*, **52**, 2567–2581, <https://doi.org/10.1175/JAMC-D-12-085.1>.
- Ulbrich, C. W., 1983: Natural variations in the analytical form of the raindrop size distribution. *J. Climate Appl. Meteor.*, **22**, 1764–1775, [https://doi.org/10.1175/1520-0450\(1983\)022<1764:NVTAF>2.0.CO;2](https://doi.org/10.1175/1520-0450(1983)022<1764:NVTAF>2.0.CO;2).
- Umeyama, A., 2016: The bootstrap dual polarimetric spectral density estimator. M.S. thesis, School of Electrical and Computer Engineering, University of Oklahoma, 228 pp.
- Unal, C. M. H., D. N. Moiseev, F. J. Yanovsky, and H. W. J. Russchenberg, 2001: Radar Doppler polarimetry applied to precipitation measurements: Introduction of the spectral differential reflectivity. *30th Conf. on Radar Meteorology*, Munich, Germany, Amer. Meteor. Soc., 316–318.
- Wang, Y., 2010: The application of spectral analysis and artificial intelligence methods to weather radar. Ph.D. thesis, University of Oklahoma, 354 pp.
- , and T.-Y. Yu, 2015: Novel tornado detection using an adaptive neuro-fuzzy system with S-band polarimetric weather radar. *J. Atmos. Oceanic Technol.*, **32**, 195–208, <https://doi.org/10.1175/JTECH-D-14-00096.1>.
- Yu, T.-Y., R. Reinoso-Rondinel, and R. D. Palmer, 2009: Investigation of non-Gaussian Doppler spectra observed by weather radar in a tornado supercell. *J. Atmos. Oceanic Technol.*, **26**, 444–461, <https://doi.org/10.1175/2008JTECHA1124.1>.
- , X. Xiao, and Y. Wang, 2012: Statistical quality of spectral polarimetric variables for weather radar. *J. Atmos. Oceanic Technol.*, **29**, 1221–1235, <https://doi.org/10.1175/JTECH-D-11-00090.1>.
- Zhang, G., J. Vivekanandan, and E. Brandes, 2001: A method for estimating rain rate and drop size distribution from polarimetric radar measurements. *IEEE Trans. Geosci. Remote Sens.*, **39**, 830–841, <https://doi.org/10.1109/36.917906>.